

Long-term coherent timing of the accreting millisecond pulsar IGR J17062–6143

PETER BULT,^{1,2} TOD E. STROHMAYER,³ CHRISTIAN MALACARIA,^{4,5} MASON NG,⁶ AND ZORAWAR WADIASINGH^{7,8,9}

¹*Department of Astronomy, University of Maryland, College Park, MD 20742, USA*

²*Astrophysics Science Division, NASA's Goddard Space Flight Center, Greenbelt, MD 20771, USA*

³*Astrophysics Science Division and Joint Space-Science Institute, NASA's Goddard Space Flight Center, Greenbelt, MD 20771, USA*

⁴*NASA Marshall Space Flight Center, NSSTC, 320 Sparkman Drive, Huntsville, AL 35805, USA**

⁵*Universities Space Research Association, Science and Technology Institute, 320 Sparkman Drive, Huntsville, AL 35805, USA*

⁶*MIT Kavli Institute for Astrophysics and Space Research, Massachusetts Institute of Technology, Cambridge, MA 02139, USA*

⁷*Astrophysics Science Division, NASA Goddard Space Flight Center, Greenbelt, MD 20771, USA*

⁸*Centre for Space Research, North-West University, Potchefstroom Campus, Private Bag X6001, Potchefstroom 2520, South Africa*

⁹*Universities Space Research Association (USRA), Columbia, MD 21046, USA*

ABSTRACT

We report on a coherent timing analysis of the 163 Hz accreting millisecond X-ray pulsar IGR J17062–6143. Using data collected with the Neutron Star Interior Composition Explorer and XMM-Newton, we investigated the pulsar evolution over a timespan of four years. We obtained a unique phase-coherent timing solution for the stellar spin, finding the source to be spinning up at a rate of $(3.77 \pm 0.09) \times 10^{-15}$ Hz/s. We further find that the 0.4–6 keV pulse fraction varies gradually between 0.5% and 2.5% following a sinusoidal oscillation with a 1210 ± 40 day period. Finally, we supplemented this analysis with an archival Rossi X-ray Timing Explorer observation, and obtained a phase coherent model for the binary orbit spanning 12 years, yielding an orbital period derivative measurement of $(8.4 \pm 2.0) \times 10^{-12}$ s/s. This large orbital period derivative is inconsistent with a binary evolution that is dominated by gravitational wave emission, and is suggestive of highly non-conservative mass transfer in the binary system.

Keywords: stars: neutron – X-rays: binaries – X-rays: individual (IGR J17062–6143)

1. INTRODUCTION

Accreting millisecond X-ray pulsars (AMXPs) are rapidly rotating neutron stars in low-mass X-ray binary (LMXB) systems. They are characterized by the fact that their millisecond rotation periods are directly apparent from their X-ray emission in the form of coherent, highly sinusoidal periodic pulsations. Such coherent pulsations are informative about the nature of the neutron star and its accretion environment (see, e.g., Di Salvo & Sanna 2020, for a review). For instance: the precise shape of the pulse waveform encodes information about the interior composition of the star (Poutanen & Gierliński 2003); tracking the pulse arrival times allows us to study the evolution of the neutron star spin and binary orbit (Hartman et al. 2008), and may be used to study accretion torque theory (Psaltis & Chakrabarty 1999) and binary evolution models (Nelson & Rappaport 2003).

A significant challenge to the study of AMXPs comes from the fact that they are transient systems. Being powered by the accretion flow, the pulsations are only

visible during X-ray outburst. For most of the known AMXPs, these outbursts last only a few days and are interspersed by several years or even decades of quiescence, which makes it difficult to establish the long-term evolution of the neutron star rotation. Additionally, the source luminosity usually changes by orders of magnitude over the course of an outburst, implying large changes in the mass accretion rate and thus in the accretion torque acting on the neutron star.

Only three AMXPs have shown outbursts that last for several years: HETE J1900.1–2455 (Kaaret et al. 2006), MAXI J0911–655 (Sanna et al. 2017a), and IGR J17062–6143 (Strohmayer & Keek 2017). The first two, however, are both intermittent pulsars; after about a month into the outburst, the coherent pulsations disappeared (Patruno 2012; Sanna et al. 2017a; Bult et al. 2019). This leaves IGR J17062–6143 (IGR J17062) as the only known AMXP to persistently exhibit accretion powered pulsations over a timescale of decades.

The observational history of IGR J17062 is somewhat unusual. The source was first discovered with INTEGRAL in 2006 (Churazov et al. 2007), and estimated to have entered outburst sometime in late 2005 or early 2006 (Remillard & Levine 2008). Since its discovery, the system has remained remarkably stable, showing a

* NASA Postdoctoral Fellow

persistent X-ray luminosity of $L_X \approx 6 \times 10^{35} \text{ erg s}^{-1}$ with little change in its intensity or spectral continuum (Degenaar et al. 2017b; van den Eijnden et al. 2018). The detection of a highly energetic intermediate duration Type I X-ray burst in 2012 identified the source as a neutron star (Degenaar et al. 2012). Similar intermediate duration bursts were observed from IGR J17062 in 2015 (Negoro et al. 2015; Iwakiri et al. 2015) and 2020 (Nishida et al. 2020) and have been attributed to helium burning with an unusually deep ignition depth (Keek et al. 2017). Equating the measured luminosity during the photospheric radius expansion phase of the 2015 X-ray burst to the empirical Eddington luminosity, Keek et al. (2017) estimated the distance to the source at $7.3 \pm 0.5 \text{ kpc}$. The 163 Hz pulsations were not discovered until 2017 from the single archival RXTE observation collected for this source in 2008 (Strohmayer & Keek 2017). The binary ephemeris was subsequently determined with NICER (Strohmayer et al. 2018), establishing that the pulsar resides in a 38-minute ultra-compact binary, as was suspected based on multi-wavelength modelling of the accretion disk emission (Hernández Santisteban et al. 2019). Notably, Strohmayer et al. (2018) measured a binary mass function of $(9.12 \pm 0.02) \times 10^{-8} M_\odot$, which is the smallest among known stellar binaries and implies a minimum companion star mass of $0.006 M_\odot$ (assuming a $1.4 M_\odot$ neutron star).

Although IGR J17062 is unique in the sense that it is the only AMXP to persistently show pulsations over decades, the long-term evolution of its pulse properties has not yet been investigated in detail. To that end, we have executed a multi-year monitoring campaign of IGR J17062 using NICER, with the aim of measuring the orbital and spin evolution of this pulsar. In this work we present a phase-coherent timing analysis of these observations. We further supplement these observations with XMM-Newton data collected in 2016 to obtain a long-term timing solution spanning 4 years, and with the 2008 RXTE observation to extend the orbital solution to 12 years.

2. OBSERVATIONS AND DATA PROCESSING

2.1. NICER

Between 2017 August and 2020 August NICER has observed IGR J17062 for a total unfiltered exposure of 372 ks. Based on their spacing in time, these data are naturally grouped into ten distinct epochs. We list these groups and their respective ObsIDs in Table 1.

We processed all data using NICERDAS version 7a, which is released with HEASOFT version 6.27.2. By default, this pipeline selects only those epochs with a pointing offset $< 54''$, a bright Earth limb angle $> 30^\circ$, a dark Earth limb angle $> 15^\circ$, and which are outside of the South Atlantic Anomaly. It additionally screens for signs of increased background emission by retaining only those data epochs that were collected at times

when the rate of reset triggers (undershoots) is $< 200 \text{ ct/s/detector}$ and the rate of high energy events (overshoots) is $< 1 \text{ ct/s/detector}$ and $< 1.52 \times \text{COR_SAX}^{-0.633}$, where COR_SAX gives the cut-off rigidity of the Earth's magnetic field. We find that these latter two criteria are often too conservative when applied to the observations of IGR J17062. Following Bult et al. (2020a), we first smoothed the overshoot light curve using 5-second windows to reduce noise and then only retained those epochs when the absolute rate was less than $1.5 \text{ ct/s/detector}$ and increased the scaling factor of the COR_SAX expression filter from 1.52 to 2.0. The undershoot filter was only an issue in data groups 3,4,5, and 8. These data were all collected at times when the Sun angle was comparatively low ($< 65^\circ$), which increases the optical load on the instrument and affects the low-energy background. We increased the undershoot rate filter for these data from $200 \text{ ct/s/detector}$ to $400 \text{ ct/s/detector}$. For all ObsIDs we compare the light curves obtained with default screening criteria to those obtained with our relaxed parameters to ensure no spurious features are introduced into the data selection.

Inspecting the light curves, we find that a number of the individual exposures in the third data group show near identical light curve profiles in which the overall count-rate drops linearly from about 40 cts^{-1} to 0 cts^{-1} . These decays coincide with a decrease in the number of stars traced by the star tracker, and reflects an obstruction of the field of view rather than being of astrophysical origin¹. We reprocessed these particular ObsID with the additional requirement that the number of stars in the star tracker (ST_STARS) be larger than 38, which effectively removed all spurious trends.

After screening our data, we are left with 202 ks of clean exposure (as opposed to the 187 ks retained under standard screening criteria). We applied barycenter corrections to these cleaned data using the Swift/UVOT position of Ricci et al. (2008) and the JPL-DE405 solar system ephemeris (Standish 1998). All dates reported in this work are therefore in terms of Barycentric Dynamic Time (TDB).

2.2. XMM-Newton

XMM-Newton observed IGR J17062 on 2016 September 13-15 (MJD 57645; see van den Eijnden et al. (2018) for a detailed analysis). This data was collected with the EPIC-PN camera in timing mode, yielding a relative time resolution of $30 \mu\text{s}$. The absolute timing calibration of XMM-Newton has an accuracy of $100 \mu\text{s}$ (Rosen 2020), which translates to a systematic phase uncertainty of 0.02 cycles for IGR J17062. Hence, these data can be used to extend the coherent timing analysis of our NICER observations.

¹ In each case these anomalies can be attributed to the ISS solar panels passing through the instrument's field of view.

Table 1. Data overview

Group	ObsID Range	Date	Exposure
1	10341001 [01 – 07]	2017-Aug	17.8
2	10341001 [08 – 10]	2017-Oct	9.8
3	10341001 [11 – 18]	2017-Nov	16.5
4	10341001 [19 – 22]	2017-Nov	2.1
5	10341001 [23 – 27]	2018-Jan	2.1
6	26010101 [01 – 04]	2019-Apr	27.5
7	26010102 [01 – 04]	2019-Jul	23.6
8	20341001 [01 – 03]	2019-Oct	16.9
9	30341001 [01 – 12]	2020-Jun	25.9
10	36120101 [01 – 11]	2020-Aug	60.1

NOTE—The rightmost column lists the clean exposure in ks.

We processed the XMM-Newton data in SAS v18 using the latest version of the calibration files. Standard screening filters were applied, i.e; we kept only those events with photon energies in the 0.4 – 10 keV range, with PATTERN ≤ 4 and screening FLAG = 0. We extracted the source event list from RAWX columns [34 : 42], and obtained background events from RAWX columns [6 : 14]. The source light curve showed a mean count-rate of 18 cts $^{-1}$ over the 61 ks exposure, with a background contribution of 0.26 cts $^{-1}$. Finally, we used BARYCEN to apply barycentric corrections to our source data, based on the same source coordinates and ephemerides used for NICER.

2.3. RXTE

RXTE observed IGR J17062 on 2008 May 3 (MJD 54589.0) for a total good time exposure of 1.1 ks in the proportional counter array (PCA). The data was collected with the PCA operating in event mode, using 64 energy channels and a time resolution of 1/8192 s. A detailed analysis of these data is presented by Strohmayer & Keek (2017). Here, we applied standard processing and screening methods to extract a photon event list for this observation, and used FAXBARY to apply barycentering corrections. The background rate was estimated using PCBACKEST.

3. NICER LIGHT CURVE

To investigate the source evolution over the span of our NICER monitoring, we split the data into intervals representing continuous NICER pointings. For each such pointing, we extracted a source spectrum and generated a background spectrum using version 6 of the 3c50 NICER background model² (Remillard et

² https://heasarc.gsfc.nasa.gov/docs/nicer/tools/nicer_bkg_est_tools.html

al., *subm.*). We find that the source emission dominates over the background between 0.4–6 keV, and compute a background subtracted light curve in that energy range (Figure 1). We find that the source count-rate remains stable over the 3 year baseline of our NICER data, varying only slowly between approximately 30 cts $^{-1}$ and 50 cts $^{-1}$. Only in data group 9 do we see a large swing in source intensity. This data, however, was collected in response to an intermediate duration X-ray burst from this source (Nishida et al. 2020). The initial spike in count-rate is due to the cooling-tail of that X-ray burst, whereas the subsequent oscillation in source rate is similar to the system response after its 2015 X-ray burst (Keek et al. 2017). A detailed analysis of this event will be presented elsewhere.

4. COHERENT TIMING

4.1. Semi-coherent searches

Following the approach of Strohmayer et al. (2018), we separately search each data group for the presence of 163 Hz pulsations by optimizing the Z_1^2 score (Buccheri et al. 1983) as a function of spin frequency and the binary orbit’s time of ascending node, T_{asc} . We adopt the ephemeris reported by Strohmayer et al. (2018) as our trial solution³, and correct the photon arrival times to remove the Doppler modulation imposed by the circular binary orbit. We then compute the Z_1^2 score as

$$Z_1^2 = \frac{2}{N} \left[\left(\sum_{j=1}^N \cos \varphi_j \right)^2 + \left(\sum_{j=1}^N \sin \varphi_j \right)^2 \right], \quad (1)$$

with $\varphi_j = 2\pi\nu_i t_j$, where the t_j give the list of N photon arrival times in a group, and ν_i is the test frequency. We evaluate this score on a grid of trial frequencies spanning $\pm 40 \mu\text{Hz}$ around the source spin frequency. The window width was conservatively chosen such that we are sensitive to a long-term spin frequency derivative smaller than $4 \times 10^{-13} \text{ Hz s}^{-1}$ over the three year span between the first and last data groups. The grid resolution is set to $1/(8T)$, where T is the duration of the respective data group, that is, the time between the first and last photon events in that group. For T_{asc} we adopt a grid spanning one orbital period that we center on the middle of the respective data group’s time interval. This grid has a resolution of 25 s, which is equivalent to 4° orbital longitude.

We applied the Z_1^2 optimization method to all data groups, excluding group 9 which is dominated by the X-ray burst response, and groups 4 and 5, which do not have sufficient exposure for this type of broadly de-

³ Note that the spin frequency reported in Table 1 of Strohmayer et al. (2018) contains a typographical error. We instead adopt the value quoted in the running text, which we independently verified to be correct.

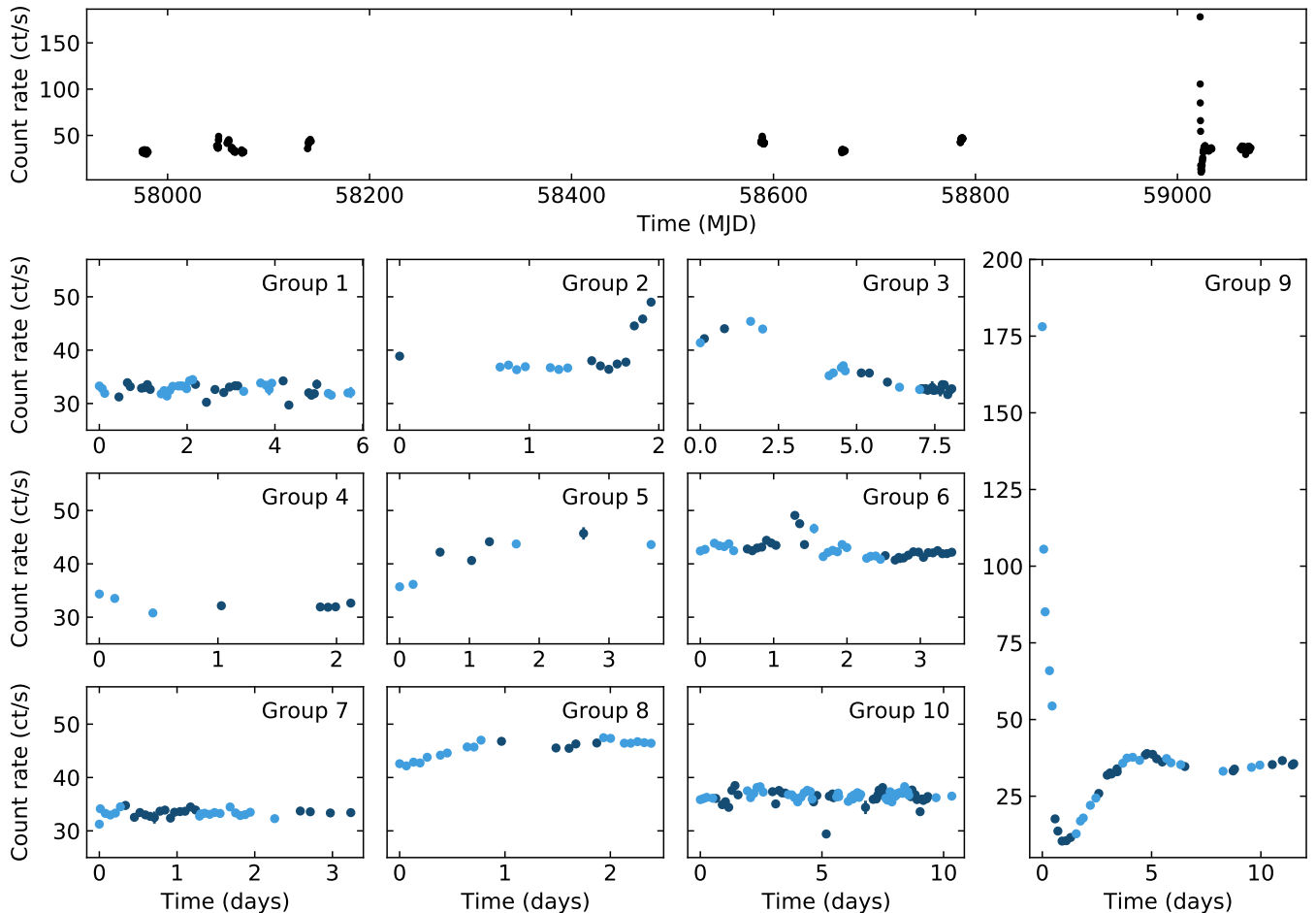


Figure 1. Background subtracted 0.3–6 keV NICER light curve of IGR J17062. The top panel shows the complete light curve, with each point giving the average of a single continuous pointing. The bottom panels show the same data, but zoomed-in on the respective data groups as labeled. We plot the zoomed panels relative to the start time of each group, and alternate the point colors to indicate the even and odd ObsID numbers. The large swing in count-rate seen in group 9 is due to an intermediate duration X-ray burst from this source (Nishida et al. 2020).

finer search. Coherent 163 Hz pulsations were recovered in all searched groups. We determined uncertainties on the resulting spin frequency and T_{asc} measurements by scanning the Z_1^2 space for the boundary interval where $\Delta Z_1^2 = 9$, which corresponds to the 3σ confidence boundaries (Markwardt et al. 2002). To further verify the validity of these parameter uncertainties, we simulated 1000 Poisson sampled event lists from the timing model while maintaining the same count rates and good time intervals as our observations. Running the Z_1^2 optimization method on these simulated data, we obtained parameter uncertainties that were entirely consistent with those found through the $\Delta Z_1^2 = 9$ interval scan. The resulting measurements and uncertainties are shown in Figure 2, with the detailed parameter values reported in the appendix.

Considering the pulse frequency measurements, we observe a modest linear drift across the data groups (Figure 2, top panel). To verify if this drift is sta-

tistically significant, we first fit the measurements using a constant frequency model. We obtain a best-fit χ^2 of 39 for 6 degrees of freedom, yielding a p-value of 7×10^{-7} . Hence, this fit firmly rejects the constant spin-frequency hypothesis. Fitting the measurements with a linear function instead, we obtain an acceptable fit, if slightly under dispersed at a χ^2 of 1.0 for 5 degrees of freedom. The best-fit parameters of this linear fit give a spin-frequency measurement of $\nu = 163.65611072 \pm 4 \times 10^{-8}$ Hz at a reference time of 58522.3 TDB, with a significantly detected long-term spin-up of $\dot{\nu} = (5.3 \pm 0.9) \times 10^{-15}$ Hz s $^{-1}$.

Considering the T_{asc} measurements, we observe a similar long-term evolution in our measurements. In Figure 2 (bottom panel) we plot the measured T_{asc} relative to the predicted values based on the constant orbital period model of Strohmayer et al. (2018). These measurements are well described using a linear function, yielding a best-fit χ^2 of 8.4 for 5 degrees of freedom. The result-

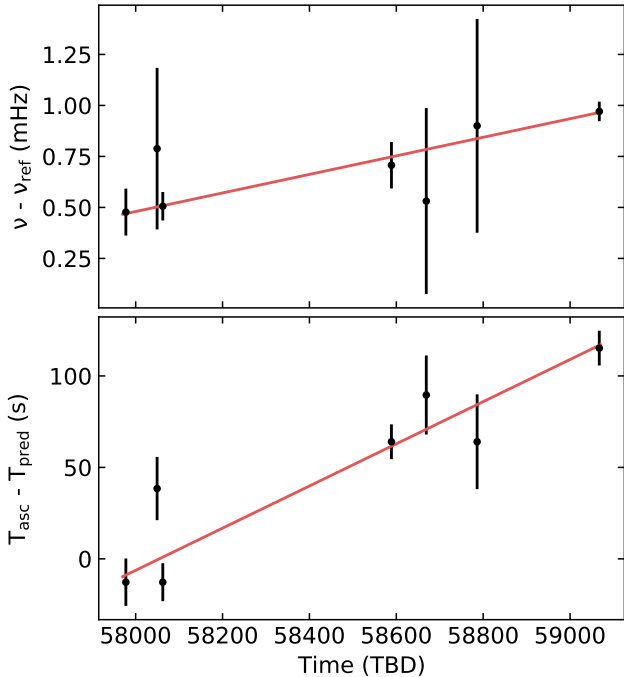


Figure 2. Individual spin frequency and T_{asc} measurements for each of the NICER data groups listed in Table 1 (excluding groups 4, 5, and 9). The top panel shows the frequency measurements in units of mHz relative to reference frequency $\nu_{\text{ref}} = 163.656110$ Hz. The bottom panel shows the residual T_{asc} relative to the constant orbital period model of (Strohmayer et al. 2018). For both panels the red line shows the best fit linear fit to the data.

ing best-fit orbital period is $P_b = 2278.2110 \text{ s} \pm 0.3 \text{ ms}$, which is 3 ms larger than the orbital period reported in Strohmayer et al. (2018) and well within their 12 ms uncertainty region. Adding a quadratic term to the model, we can further place a 95% confidence upper limit on the long-term derivative of the orbital period of $|\dot{P}_b| < 10^{-11} \text{ s s}^{-1}$.

Using spin frequency and binary period parameters obtained from these linear models, we refined the timing solution, and extrapolate the ephemeris to the epoch of the XMM-Newton observation. We then selected the 0.4–6 keV events and corrected their arrival times to the pulsar’s reference frame using this predicted ephemeris. Calculating the Z_1^2 score for this data, we obtain a score of $Z_1^2 = 18$, which has an associated single trial p-value of 1×10^{-4} . Hence, the pulsations are significantly detected in the XMM-Newton observation at the 4σ level.

We also used the interim timing solution to consider NICER data groups 4, 5, and 9. In each case we corrected the arrival times for the predicted binary orbit and determined the Z_1^2 score. Significant pulsations we recovered in groups 4 (p-value of 3×10^{-4} ; 3.6σ) and 5 (p-value of 7×10^{-6} ; 4.5σ), but not in group 9 (p-value of 0.77). Because the source luminosity varies drastically

across data group 9, we also searched each individual ObsID, however this did not yield a pulse detection either. Finally, we attempted to suppress the influence of the X-ray burst by processing the data in reverse order. That is, we first searched the last ObsID for pulsations. As none were detected, we added the second-to-last and-so-forth. At no point in this process did the pulse significance exceed 1σ . In the absence of a detection, we calculate a 95% confidence level upper limit on the pulse fraction of 0.8% if we include all ObsIDs in this group. We note, though, that this limit relaxes to 1.1% if exclude the first four ObsIDs, which show the largest swing in source intensity (see Figure 1).

4.2. Fully coherent pulse timing

A fully coherent description of the pulse signal requires that our timing solution is precise enough to exactly predict the number of orbital revolutions and stellar rotations that take place during the time intervals between the data groups. Adopting the interim timing solution obtained in the previous section, we find that the orbital phase is readily extrapolated across the time span of our data (as is clear from Figure 2). The stellar rotation, on the other hand, requires more attention. The uncertainty in the predicted pulse phase grows approximately as

$$\sigma_\phi^2(t) = (\sigma_\nu t)^2 + \left(\frac{1}{2}\sigma_{\dot{\nu}}t^2\right)^2, \quad (2)$$

where σ_ν gives the uncertainty on the spin frequency and $\sigma_{\dot{\nu}}$ gives the uncertainty on its derivative. Using the uncertainties obtained in Section 4.1, we find that the timing solution loses coherence (σ_ϕ exceeds 0.5), when $t \approx 200$ days. Hence, we can coherently connect some data groups, but not all of them at once. To further refine the timing solution, we therefore start by combining data groups 2, 3, and 4, which have the shortest time intervals between them. For each group, we fold the data to a pulse profile, which we fit with a sinusoid to measure the pulse phase residual relative to the model. The set of phase residuals are then modeled using a quadratic function, so that we obtain refined measurements for ν and $\dot{\nu}$, thus increasing the coherence time. By iteratively adding the nearest data group to the analysis, we gradually converge to a single timing solution that coherently describes all data. This approach yielded a final spin frequency of $\nu = 163.6561106613 \pm 1.0 \times 10^{-9}$ Hz and a derivative of $\dot{\nu} = (3.73 \pm 0.07) \times 10^{-15}$ Hz s $^{-1}$ measured relative to a spin epoch of 58522.3 TDB.

While the iterative approach allowed us to determine a coherent solution for the whole data set, this method is at risk of converging to a local minimum if the timing solution is not unique. To verify the uniqueness of the solution, we took a numerical approach. We scanned through the joint 5σ confidence region in ν and $\dot{\nu}$ while taking steps of 10^{-10} Hz in frequency space and steps of 10^{-18} Hz s $^{-1}$ in the derivative. For each trial we compute the phase-residuals for the XMM-Newton observa-

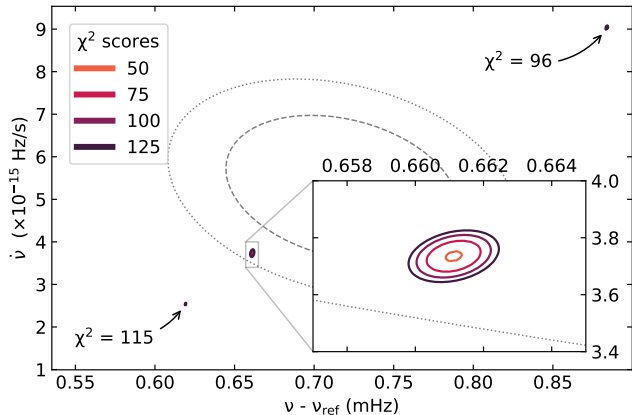


Figure 3. Phase-residual χ^2 -space as a function of spin frequency and spin frequency derivative. The grey dashed and dotted ellipses show the 2σ and 3σ constraints obtained in Section 4.1. The four colored contours map out χ^2 levels of 50, 75, 100 and 125, which correspond to p-values of approximately 10^{-10} , 10^{-15} , 10^{-20} , and 10^{-25} , respectively. Only one high-probability minimum is found (minimum $\chi^2 = 41$), with the inset showing a zoom-in of this region.

tion and each of the NICER data groups (excluding only group 9), and calculate the χ^2 of this model. As shown in Figure 3, this χ^2 scan yielded only one plausible timing solution, which had the same $(\nu, \dot{\nu})$ parameters found previously through the iterative approach.

We adopted the spin frequency and spin frequency derivative measurements associated with the minimum in χ^2 space and constructed the phase residuals. We then fit these residuals jointly for the frequency evolution and the binary orbit parameters (orbital period, projected semi-major axis, and T_{asc}). This fit yielded a slightly improved description of the pulse arrival times and higher precision measurements of the orbital parameters. We further attempted adding a second frequency derivative to the model, but this did not improve the fit. Including orbital eccentricity or a binary period derivative was not required either. Finally, optimizing the pulse phase residuals as a function of the source coordinate did not improve the residuals either, suggesting the source position is correct to within a 90% confidence uncertainty region of $0.1''$. The complete timing model is listed in Table 2, while the resulting phase residuals are shown in Figure 4.

Using the refined timing solution, we can revisit the 2008 RXTE observation to test for consistency. Extrapolating the spin frequency and T_{asc} to the RXTE epoch (54589.5 TDB) and folding these data, we measure a pulse fraction of about 7%. Given that Strohmayer & Keek (2017) report a pulse fraction of 9%, this result indicates our timing solution is still suboptimal. We therefore optimized the local timing solution by again determining the peak Z_1^2 score as a function of the

Table 2. NICER timing solution

Parameter	Value	Uncertainty
R.A. (J2000)	17:06:16.29	$0.1''$
Decl. (J2000)	-61:42:40.6	$0.1''$
ν (Hz)	163.6561106623	1.0×10^{-9}
$\dot{\nu}$ (Hz s^{-1})	3.77×10^{-15}	9×10^{-17}
$ \ddot{\nu} $ (Hz s^{-2})	$< 1.3 \times 10^{-24}$	
Spin epoch	58522.3	
P_b (s)	2278.21124	2×10^{-5}
\dot{P}_b (ss^{-1})	8.4×10^{-12}	2×10^{-12}
Semi-major axis (lt-s)	0.003963	6×10^{-6}
T_{asc} (TDB)	58588.78464	5×10^{-5}
Eccentricity	< 0.03	

NOTE—Source coordinates were adopted from Ricci et al. (2008), with improved uncertainties obtained through the timing model. Upper limits are quoted at 95% confidence.

time of ascending node and the spin frequency, finding $T_{\text{asc}} = 54589.5510 \pm 0.0003$ TDB and $\nu = 163.65612 \pm 5 \times 10^{-5}$ Hz. This frequency measurement is consistent with the long-term frequency solution, deviating only by 0.1σ . The time of ascending node, on the other hand, arrives 233 seconds later than predicted, which constitutes a 3.3σ shift. Combining this measurement with the T_{asc} values obtained from NICER and XMM-Newton, we find that the long-term drift in T_{asc} is incompatible with a linear trend ($\chi^2/\text{dof} = 25.9/7$), but well described by a quadratic function ($\chi^2/\text{dof} = 8.9/6$). The binary period derivative obtained through this fit is $\dot{P}_b = (8.4 \pm 2.0) \times 10^{-12} \text{ ss}^{-1}$, indicating that the binary orbit is expanding. The reference T_{asc} and orbital period obtained through this fit are consistent with those found previously (to within 1σ).

4.3. Pulse variability

Considering the pulse amplitudes across the different data groups, we observe clear evolution in pulse fraction over time. This trend could be well described as a sinusoid ($\chi^2/\text{dof} = 6.4/6$), yielding an amplitude of $(1.25 \pm 0.16)\%$ over a mean pulse fraction of $(1.94 \pm 0.08)\%$, with a period measurement of 1210 ± 40 days, or about 3.3 years (see Figure 4). The $1 - 10$ keV X-ray flux of these data groups does not exhibit any such oscillation, instead showing a random 13% rms scatter around a mean flux of $\approx 6 \times 10^{-11} \text{ erg s}^{-1} \text{ cm}^{-2}$.

To investigate the energy dependence of the pulsations, we folded all NICER data to pulse profiles in several energy bins spanning $0.4 - 10$ keV. The bins were constructed adaptively to be multiples of 0.5 keV, such that each bin contained at least 10^4 counts and the pulsation was detected at $> 5\sigma$ significance. As shown in

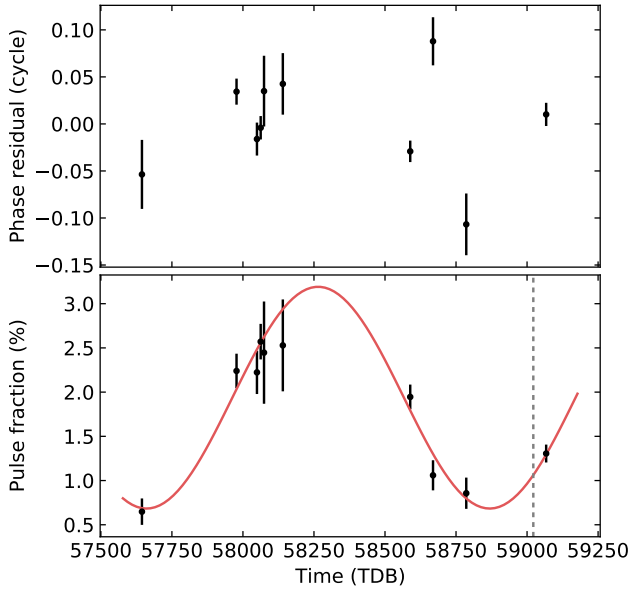


Figure 4. Pulse properties as a function of time. The top panel shows the pulse phase residuals relative to the timing model reported in Table 2. The bottom panel shows the pulse fraction of the fundamental pulsation, along with a best-fit sinusoidal model (red). The sinusoid has an amplitude of $(1.25 \pm 0.16)\%$ over a mean of $(1.94 \pm 0.08)\%$ and a period of 1210 ± 40 days. The vertical dashed line indicates the time of the 2020 intermediate duration X-ray burst.

Figure 5, we find that the time-averaged fractional pulse amplitude increases with energy to a peak of about 4.5% between 5–10 keV. For the pulse phase, we find that the pulsations have a roughly constant phase below 2 keV, but show an decreasing phase-lag toward higher energies, i.e. the softer photons (< 2 keV) tend to arrive after the harder photons (> 2 keV).

For comparison, we also calculated the energy dependence of the pulse detection in the 2008 RXTE observation. Using the local timing solution, we adaptively binned individual event channels such that each bin contained a pulse detection of at least $> 5\sigma$. We find the pulsations could be resolved in five separate energy bins, which are shown in Figure 5 using red diamonds.

5. SPECTROSCOPY

The pulse-phase averaged X-ray spectrum of IGR J17062 has been studied in detail by Degenaar et al. (2017b), Keek et al. (2017), and van den Eijnden et al. (2018). These studies have consistently found that the continuum emission is well described by a phenomenological model consisting of a single temperature blackbody with a power law tail toward high energy, and a Gaussian emission line centered at 1 keV.

In order to verify if this three component spectral model is appropriate for the NICER data as well, we extracted a 0.4–6.0 keV spectrum for each of the NICER

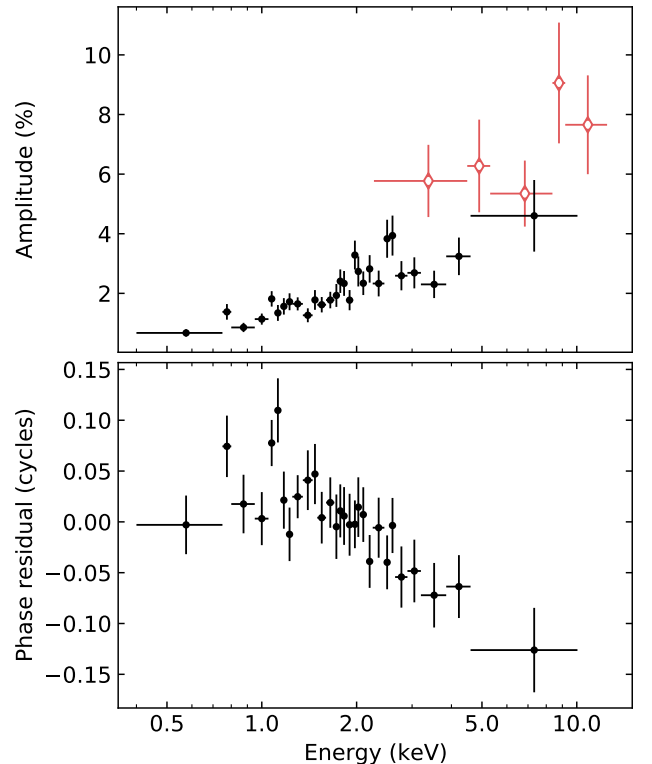


Figure 5. Pulse properties of IGR J17062 as a function of photon energy, showing the pulse amplitude in the top panel and the pulse phase in the bottom panel. Solid black points show NICER data and open red diamonds show the RXTE measurements. The phases are expressed relative to the 0.4–6 keV energy band model reported in Table 2.

data groups (excluding group 9). We model these spectra in XSPEC v12.11 (Arnaud 1996) using the Tübingen-Boulder interstellar absorption model (Wilms et al. 2000). We find that the three component model gives a reasonable description for the continuum emission in all groups, with best-fit spectral parameters that are consistent within their respective uncertainties across the data groups. The model parameters (see the appendix for detailed values) are broadly consistent with those reported by van den Eijnden et al. (2018) based on 2015 Swift/XRT data and the 2016 XMM-Newton observation. The largest offset is found in the power law photon index, where we measure a value of ≈ 1.8 versus the 2.0 and 2.1 reported by van den Eijnden et al. (2018). This difference is likely an effect of the energy passband, however, as our NICER spectra have a comparatively low upper bound of 6 keV, so that our sensitivity to the power law emission is quite poor.

Having established that the phase averaged spectra do not vary substantially across the different data groups, we proceeded with the phase-resolved analysis. Using the coherent timing solution obtained in Section 4.2, we assigned a rotational phase to each measured pho-

Table 3. Phase-resolved spectroscopy

Component	Parameter	Value	
Absorption	N_H	$(0.110 \pm 0.003) \times 10^{22} \text{ cm}^{-2}$	
Gaussian	line flux	$(1.59 \pm 0.09) \times 10^{-12} \text{ erg s}^{-1} \text{ cm}^{-2}$	
Gaussian	line energy	$0.961 \pm 0.006 \text{ keV}$	
Gaussian	line sigma	$0.182 \pm 0.009 \text{ keV}$	
Blackbody	mean kT	$0.421 \pm 0.002 \text{ keV}$	
Blackbody	mean norm	$77.5 \pm 1.2 (\text{km} / 10 \text{ kpc})^2$	
Power law	mean index	1.831 ± 0.003	
Power law	mean flux	$(4.22 \pm 0.02) \times 10^{-11} \text{ erg s}^{-1} \text{ cm}^{-2}$	
Component	Parameter	Amplitude	Phase
Blackbody	kT	$(1.3 \pm 0.5)\%$	0.38 ± 0.06
Blackbody	norm	$(2.7 \pm 2.1)\%$	0.85 ± 0.12
Gaussian	flux	$(5.5 \pm 3.6)\%$	0.47 ± 0.11
Power law	index	$(0.4 \pm 0.2)\%$	0.65 ± 0.10
Power law	flux	$(1.6 \pm 0.5)\%$	0.21 ± 0.05

NOTE—Flux measurements correspond to the 1 – 10 keV band. Uncertainties are quoted at 90% confidence.

ton. We then stacked all available data, and extracted 0.4 – 6.0 keV spectra in 8 separate phase bins. We modelled these 8 spectra jointly using the same three component model used for the phase-averaged spectra. Initially, we let all model parameters vary, keeping only the absorption column density tied across the phase spectra. This fit yielded a good description of the continuum, with all parameters in the same range as found from the phase-averaged analysis. Considering the obtained spectral parameters as a function of phase bin, we could observe an apparent oscillation in several spectral parameters (see Figure 6). We modelled these variations using a sinusoidal model, requiring the sinusoidal amplitude to be greater than three times its uncertainty for a significant detection. The modulation in the blackbody temperature and power law flux were thus found to be significant, at 4.3σ and 5.2σ , respectively. Additionally, we found marginal oscillations in the blackbody normalization (2.1σ), the power law photon index (2.7σ), and the Gaussian line flux (2.5σ). The line energy and width did not show signs of phase dependence ($< 1\sigma$). The spectral and sinusoidal parameters are reported in Table 3.

6. DISCUSSION

We have presented a timing analysis of the 163 Hz pulsations of IGR J17062 using NICER and XMM-Newton observations spanning four years. We found that these data could be described with a coherent timing solution, allowing us to measure the positive spin frequency derivative. Additionally, we studied the time and energy dependence of the pulsations, finding the pulse amplitude to vary slowly with time, suggesting a years-long oscillation. Supplementing these data with a 2008 RXTE observation, we obtained a coherent model for the bi-

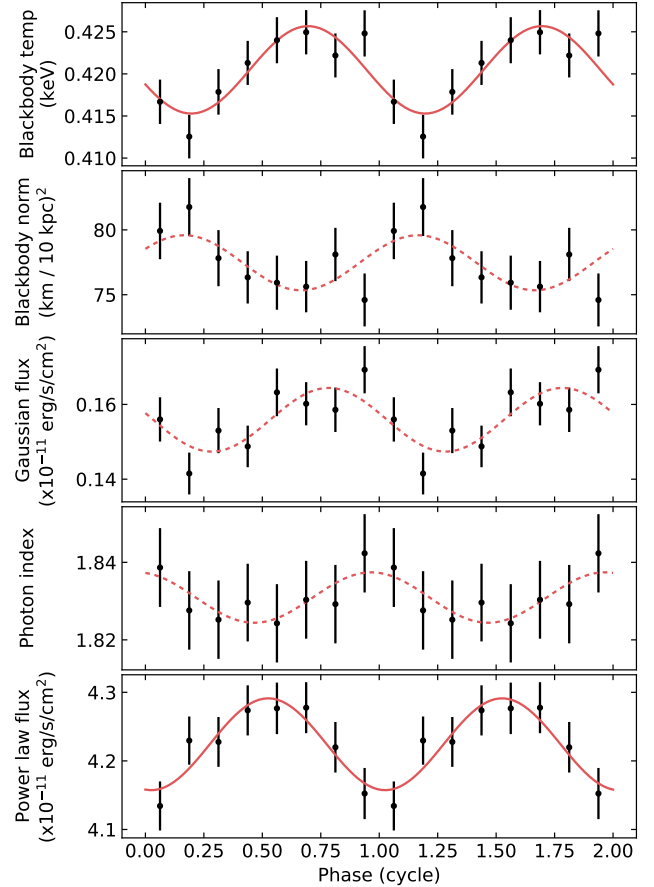


Figure 6. Phase resolved spectroscopic parameters of IGR J17062, showing from top to bottom: the blackbody temperature, the blackbody normalization, the Gaussian line flux, the power law photon index, and the power law flux. Both flux measurements are obtained for the 1 – 10 keV energy band. In each panel we show the respective spectral parameter across two rotation cycles (black), along with the best fit sinusoidal model (red). We use a solid line where the spectral parameter shows a significant pulsation ($> 3\sigma$), and a dashed line where the parameter pulsation is marginal ($2 - 3\sigma$). The remaining spectral parameters were held tied across the phase bins, with all model parameters listed in Table 3.

nary orbit spanning 12 years and a measurement of the binary period derivative. In the following we discuss the implications of these measurements.

6.1. Long-term spin up

We have measured the long-term spin frequency derivative of IGR J17062 to be $\dot{\nu} = (3.73 \pm 0.03) \times 10^{-15} \text{ Hz s}^{-1}$, indicating the neutron star is slowly spinning up under the influence of sustained mass accretion onto the star. Positive pulse frequency derivatives have been previously reported for several other AMXPs during outburst (Di Salvo & Sanna 2020), with magnitudes

on the order of $10^{-14} \sim 10^{-13} \text{ Hz s}^{-1}$. In all cases these derivatives were measured by modelling the quadratic drift in pulse phase. However, flux-dependent timing noise can bias such phase measurements, making it difficult to disentangle what part of the observed phase drift is intrinsic to the pulsar rotation and what part is instead due to accretion driven variability in the hot spot (Patruno et al. 2009; Bult et al. 2020a). Our spin frequency derivative measurement for IGR J17062 does not suffer from this ambiguity: the spin change is directly visible in frequency space.

In the conventional picture of accretion onto a magnetized star, the spin evolution of the star is governed by the interaction between the stellar magnetosphere and the inner accretion disk. The stellar magnetic field truncates the accretion disk at r_m , the magnetospheric radius. Just outside r_m , the field threads the disk leading to an exchange of angular momentum between the star and the accretion flow that depends on the difference in their angular velocities. While the precise torques acting on the star depend on the specifics of the interaction model, the torque is generally expressed as

$$N_{\text{total}} = \dot{M}_{\text{ns}} \sqrt{GM_{\text{ns}} r_m} + N_{\text{field}}, \quad (3)$$

where \dot{M}_{ns} is the mass accretion rate onto the neutron star, G the gravitational constant, and M_{ns} the mass of the neutron star. The N_{field} term expresses the torque exchange between the magnetosphere and the inner accretion disk, and depends on specific assumptions about the microphysics of the magnetic coupling. Rappaport et al. (2004) studied the specific case of an accretion disk around a millisecond pulsar, and derived

$$N_{\text{field}} = \begin{cases} \frac{\mu^2}{3r_c^3} \left[\frac{2}{3} - 2 \left(\frac{r_c}{r_m} \right)^{3/2} + \left(\frac{r_c}{r_m} \right)^3 \right] & r_m < r_c, \\ -\frac{\mu^2}{9r_c^3} & r_m > r_c \end{cases}$$

where μ is the magnetic dipole moment and

$$r_c = \left(\frac{GM_{\text{ns}}}{\Omega_s^2} \right)^{1/3}, \quad (4)$$

the corotation radius, with $\Omega_s = 2\pi\nu$ the angular velocity of the neutron star. Adopting a $1.4M_{\odot}$ neutron star, we find that the corotation radius of IGR J17062 is 56 km.

The measured spin frequency derivative gives us a measure of the total torque acting on the star as $N_{\text{total}} = 2\pi I \dot{\nu}$, where $I = (0.5 - 2) \times 10^{45} \text{ g cm}^2$ gives the neutron star moment of inertia (Friedman et al. 1986; Steiner et al. 2015). Substituting this expression into equation 3, we can place a lower limit on the magnetic dipole moment of $\mu \geq 1 \times 10^{26} \text{ G cm}^3$, with a magnetospheric radius of $r_m \geq 50 \text{ km}$. We can obtain more precise measurements if we further assume that the magnetospheric

radius scales with the mass accretion rate as

$$r_m = \xi \left(\frac{\mu^4}{GM_{\text{ns}} \dot{M}^2} \right)^{1/7}, \quad (5)$$

with scaling factor $\xi \approx 0.5$ (Long et al. 2005; Bessolaz et al. 2008; Zanni & Ferreira 2013). Assuming the X-ray flux is a good tracer of the mass accretion rate, we adopt the 0.3 – 79 keV luminosity measured by van den Eijnden et al. (2018) to find that the accretion rate onto the neutron star is $\dot{M}_{\text{ns}} = 2.5 \times 10^{-11} M_{\odot} \text{ yr}^{-1}$. Considering the energetics and recurrence time of the X-ray bursts, Keek et al. (2017) derive a similar accretion rate, suggesting that this estimate is quite robust. Solving the set of equations gives $\mu = 2.9 \times 10^{26} \text{ G cm}^3$ with a truncation radius of 52 km.

Obviously the derived dipole moment is highly model dependent, as somewhat different prescriptions of the disk-field interaction will produce slightly different outcomes. There may also be additional torques acting on the neutron star, such as the torque associated with a propeller mechanism (Illarionov & Sunyaev 1975). There is reason to suspect that a propeller mechanism might be active in IGR J17062; for one, the mass flow rate through the accretion disk has been estimated to be $1.8 \times 10^{-10} M_{\odot} \text{ yr}^{-1}$ (Hernández Santisteban et al. 2019), about on order of magnitude higher than the accretion rate onto the neutron star. Additionally, high resolution X-ray spectroscopy (Degenaar et al. 2017b; van den Eijnden et al. 2018) revealed narrow emission lines, which can be interpreted as the blueshifted emission of an outflow. If we assume that IGR J17062 is in a weak propeller regime (Romanova et al. 2005; Ustyugova et al. 2006), then part of the accretion flow is ejected by the propeller, and the remainder accretes onto the neutron star. In this case, the material pressure exerted on the magnetosphere can be much greater than inferred from the X-ray flux, while the ejection mechanism itself applies a negative torque to the neutron star. The torque equation becomes

$$N_{\text{total}} = \dot{M} \sqrt{GM_{\text{ns}} r_m} + N_{\text{field}} + N_{\text{propeller}}, \quad (6)$$

where

$$N_{\text{propeller}} = \dot{M}_{\text{ej}} \sqrt{GM_{\text{ns}} r_m}, \quad (7)$$

with $-\dot{M}_{\text{ej}} = \dot{M}_{\text{disk}} - \dot{M}_{\text{ns}} < 0$ expressing the rate at which mass is being propelled out of the system. If we assume that the magnetospheric radius depends on \dot{M}_{disk} , we can again solve the equation to find $\mu = 6.3 \times 10^{26} \text{ G cm}^3$ at a radius of 46 km.

Whether we include a propeller torque or not, we therefore find that the observed spin-up of the neutron star is consistent with a stellar magnetic field of $B \approx 5 \times 10^8 \text{ G}$ and an accretion disk that is truncated close to the corotation radius. Here it is interesting to note that X-ray reflection spectroscopy of the Fe $K\alpha$

emission line is subject to a degeneracy between the inner truncation radius of the disk and the system inclination (van den Eijnden et al. 2018). Hence, if we use the truncation radius obtained from the torque analysis to break this degeneracy, the system inclination would have to be $30^\circ \sim 35^\circ$.

6.2. Binary evolution

By modelling the advancement in the time of ascending node passages between 2008 and 2020, we obtained a binary period derivative measurement of $\dot{P}_b = (8.4 \pm 2.0) \times 10^{-12} \text{ s s}^{-1}$. Hence, we find that the binary orbit is expanding with an evolutionary timescale of $P_b/\dot{P}_b = 8.6 \text{ Myr}$.

The apparent binary evolution of IGR J17062 is much faster than expected from theory. Generally, the mass transfer in an ultra-compact binary is believed to be driven by angular momentum losses through gravitational wave emission (Kraft et al. 1962), causing the binary orbit to gradually widen with time. The expected binary period derivative follows as (Rappaport et al. 1987; Verbunt 1993; di Salvo et al. 2008)

$$\dot{P}_b = 4.4 \times 10^{-14} \left(\frac{M_{\text{ns}} M_c}{M_\odot} \right) \left(\frac{M_{\text{total}}}{M_\odot} \right)^{-1/3} \times \left(\frac{P_b}{1 \text{ hr}} \right)^{-5/3} \frac{n - 1/3}{n + 5/3 - 2q} \text{ s s}^{-1}, \quad (8)$$

with M_c the mass of the companion star, $q = M_c/M_{\text{ns}}$ the binary mass ratio, and n the index of the companion star's mass-radius relation ($n = -1/3$ for a degenerate star). Adopting a $1.4 M_\odot$ neutron star and a 30° inclination (see Section 6.1), we find a companion mass of $M_c = 0.011 M_\odot$ from the mass function (Strohmayer et al. 2018), and obtain an expected orbital period derivative for IGR J17062 of $10^{-15} \text{ s s}^{-1}$, which is clearly inconsistent with our measurement.

Similarly rapid orbital evolution has been observed in a number of other AMXPs and LMXBs (Patruno et al. 2017; Di Salvo & Sanna 2020). In a few particularly well sampled sources, most notably SAX J1808.4–3658 (Bult et al. 2020a), the advancing T_{asc} shows complex residuals, suggesting that the orbital period evolution is modulated (quasi-) periodically over decades. In IGR J17062, such modulation is not apparent in the data. As the period derivative measurement is strongly influenced by the data gap between the 2008 RXTE and 2016 XMM-Newton observations, however, we note that further monitoring is required to assess the stability of the period change.

Various models have been proposed to explain the anomalously rapid evolution observed in some X-ray binaries, most prominently: donor mass loss, spin-orbit coupling, and enhanced magnetic braking (see, e.g., di Salvo et al. 2008; Burderi et al. 2009; Patruno et al. 2017; Sanna et al. 2017b, for in-depth discussions). Each

of these models, however, faces some challenges. Spin-orbit coupling relies on the presence of a variable mass quadrupole in the companion star (Applegate & Shaham 1994; Richman et al. 1994), however, a low-mass companion likely does not have a sufficient energy budget for this mechanism (Brinkworth et al. 2006), which is only exacerbated for IGR J17062, which has the smallest known mass function among stellar binaries (Strohmayer et al. 2018). Enhanced magnetic braking might play a role (Justham et al. 2006; Ginzburg & Quataert 2020), but only if the companion star can sustain a $\sim 1 \text{ kG}$ magnetic field and is also losing mass through a stellar wind. In the following, we therefore limit our discussion to just the mass loss model.

If we assume that mass transfer is non-conservative, then the matter being ejected from the binary system can carry away additional orbital angular momentum. Assuming that this mass ejection channel dominates the evolution timescale, the binary period derivative is, to good approximation, given by the relation (Rappaport et al. 1987)

$$\frac{\dot{P}_b}{P_b} = -\frac{\dot{M}_c}{M_c},$$

so that the required mass loss rate in the companion star must be $\dot{M}_c \approx 2 \times 10^{-9} M_\odot \text{ yr}^{-1}$.

As we observe an ongoing outburst from IGR J17062, at least some of the matter lost from the companion must be transferred to the neutron star. Following Rappaport et al. (1982, 1983), we can assume that a fraction $(1 - \beta)$ of the matter lost by the companion is ejected from the system, carrying specific angular momentum α , expressed in units of the companion star's orbital angular momentum. The remainder of the mass loss is transferred to the neutron star/accretion disk, so we can write $\dot{M}_{\text{disk}} = -\beta \dot{M}_c$, where the mass flow rate through the disk has been observationally constrained to $\dot{M}_{\text{disk}} = 1.8 \times 10^{-10} M_\odot \text{ yr}^{-1}$ (Hernández Santisteban et al. 2019). Hence, about 90% of the mass lost by the donor will be immediately ejected, while the remaining 10% will pass through the disk and move toward the neutron star. Given that the mass accretion rate onto the neutron star is another order of magnitude lower (Keek et al. 2017; van den Eijnden et al. 2018; Strohmayer et al. 2018), it seems that most of the matter flowing through the disk will eventually also be ejected. This secondary outflow, however, likely occurs as a disk wind or a propeller, meaning that the specific orbital angular momentum it carries is that of the neutron star ($\alpha_{\text{ns}} \approx (a_1/a_2)^2 = 0.01$) rather than that of the companion star ($\alpha \approx 1$). Hence, the impact of the second outflow on the binary evolution is expected to be negligible. Under these assumptions, the mass loss rate of the companion is given as (Rappaport et al. 1983; Verbunt 1993)

$$\dot{M}_c = \frac{32G^3}{5c^5} \left(\frac{4\pi^2}{G} \right)^{4/3} \left(\frac{M_{\text{ns}}}{P_b} \right)^{8/3} \frac{q^2}{(1+q)^{1/3} f_r}, \quad (9)$$

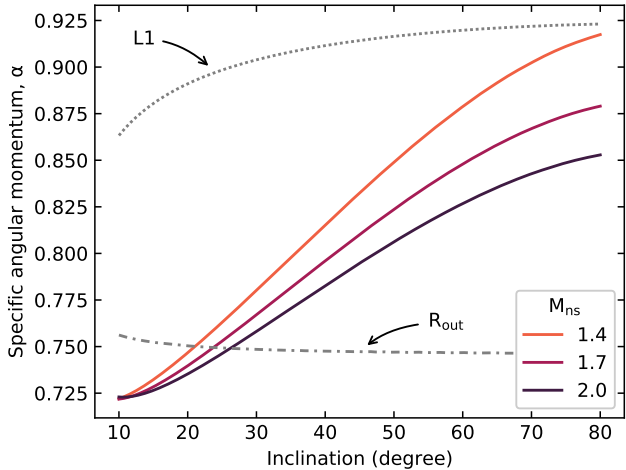


Figure 7. Specific angular momentum carried by the companion outflow, α , expressed in units of the companion star’s specific angular momentum as obtained by solving equation 9. We show α as a function of system inclination for three neutron star masses. We also show the specific orbital angular momentum of the inner Lagrange point (dotted line) and the outer edge of the accretion disk (dash-dotted), where the accretion disk radius was obtained from Hernández Santisteban et al. (2019).

where

$$f_r = \frac{5}{6} + \frac{n}{2} - \beta q - \frac{(1 - \beta)(3\alpha + q)}{3(1 + q)}. \quad (10)$$

Equating this expression to the mass loss rate implied by the orbital period derivative, we can solve for α as a function of just the neutron star mass and system inclination (Figure 7). We find $\alpha = 0.72 - 0.91$, which corresponds to an ejection radius whose specific orbital angular momentum lies somewhere between the specific orbital angular momentum carried by the outer edge of the accretion disk (~ 0.75) and that of the inner Lagrange point (~ 0.9).

What remains unaddressed, is what is powering this large mass loss rate. One possibility is that the required energy is injected via the irradiation of the donor by the luminosity generated by the neutron star. For IGR J17062, the accretion luminosity is about $6 \times 10^{35} \text{ erg s}^{-1}$. Assuming isotropic emission, the fraction of radiation intercepted by the companion star is $f = (R_c/2a)^2 = 0.23\%$, giving an irradiation rate of $\dot{E}_{\text{irr}} = 1.3 \times 10^{33} \text{ erg s}^{-1}$. The induced mass loss rate can be estimated as

$$\dot{M} = -\eta \dot{E}_{\text{irr}} \frac{R_c}{GM_c}, \quad (11)$$

so that $\eta \approx 3\%$ of the impinging energy must be converted into the kinetic energy of the wind. In practice, this efficiency should be considered a lower bound, as

the companion star is likely shadowed by the accretion disk, and any anisotropy in the accretion luminosity is unlikely to beam the emission into the orbital plane. Whether or not this efficiency is realistic is not clear, as the efficiency expected from theory will depend greatly on the energy spectrum of the wind-driving radiation and the geometry of the companion star. Typically assumed efficiencies range from 0.01-10% (Tavani & London 1993; Justham et al. 2006; Ginzburg & Quataert 2020), so it seems that the efficiency required to drive a wind in IGR J17062 is at least plausible, if on the high side.

Finally, we note that Strohmayer et al. (2018) derive a system inclination of $19^\circ - 27.5^\circ$ based on the assumption that the binary evolves on the timescale of gravitational wave emission. Clearly, this assumption cannot be correct, so that the constraint on the inclination does not hold either.

6.3. Phase resolved spectroscopy

Consistent with previous spectral analyses of IGR J17062 (Degenaar et al. 2017b; Keek et al. 2017; van den Eijnden et al. 2018), we found that the NICER data were well described using a phenomenological model consisting of an absorbed blackbody and power law, with an additional Gaussian emission line centered at 1 keV. Resolving the energy spectra as a function of the pulsar rotational phase, we find a significant pulse modulation in the blackbody temperature and the power law flux. Additionally, we found marginal evidence ($2 - 3\sigma$) for modulation in the blackbody normalization, the Gaussian line flux, and in the power law photon index.

One should be careful not to over interpret the results from phase-resolved spectroscopy. The adopted spectral model is entirely phenomenological, and likely does not fully reflect the physical processes underlying the observed emission. A more robust analysis of the phase-resolved spectroscopy requires detailed waveform modelling (see, e.g., Salmi et al. 2018), which is well beyond the scope of this work. With that caveat in mind, however, we note that the significant temperature oscillation of the blackbody component does support the interpretation that this thermal emission component is associated with the stellar surface (van den Eijnden et al. 2018; Hernández Santisteban et al. 2019).

A potentially quite interesting aspect of the phase-resolved spectroscopy is that there is some (weak) evidence that the Gaussian line flux is modulated at the stellar rotation rate. The precise origin of this emission line is not known, but it is likely with either Fe-L band emission, or possibly with a Ne X line (Degenaar et al. 2013). High resolution spectroscopy indicates the 1 keV feature can be resolved into several narrow lines (Degenaar et al. 2017b; van den Eijnden et al. 2018), and might be attributed to a collisionally ionized plasma, possibly from a shock in the accretion column. Alter-

natively, the line might be due to a blue-shifted emission line in an outflow, or from an accretion disk reflection feature (Degenaar et al. 2017b; van den Eijnden et al. 2018). A possible phase dependence of the line flux would offer interesting context to this debate. If the line originates in a shock, then one would indeed expect that the line be modulated by the stellar rotation, in which case the precise phase delay and waveform of the line flux should carry information on the precise location of that shock. Alternatively, if the line is associated with an outflow or a reflection feature, we can hypothesize that a phase dependence arises indirectly from the beamed pulsar emission sweeping periodically over the disk (or outflow), opening an opportunity for a tomographic reflection study of the accretion flow (see, e.g., Ingram et al. 2017). Given the long-term stability of its pulsations, the data quality of the energy resolved pulsations can in principle be improved with further observations. Hence, we suggest that IGR J17062 is an especially interesting target for continued monitoring and detailed pulse waveform modelling.

6.4. *The variable pulse amplitude*

Considering the pulse amplitudes measured in each of the separate observing epochs between 2016 and 2020, we found that the 0.4 – 6 keV pulse fraction of IGR J17062 ranges from 0.5% to 2.5% following a slow evolution with time. This evolution could be well described by a simple sinusoidal oscillation, yielding a period measurement of 1210 ± 40 days. Because we only observed a little over a single cycle, we could not determine if this apparent modulation is maintained over decades, nor if the oscillation is periodic or quasi-periodic.

The 2008 RXTE observation does not yield any useful constraints on the long-term pulse amplitude evolution. While the 2 – 12 keV pulse amplitude of the RXTE observation has a much higher pulse fraction of $9.4 \pm 1.1\%$ (Strohmayer & Keek 2017), we found that this measurement is strongly dependent on photon energy (Figure 5). At 2 keV the pulse fraction drops to only $6 \pm 1\%$. If we compare this to the time-averaged pulse fraction found with NICER, we see that the measurements are consistent within the statistical uncertainty. What little tension still remains between NICER and RXTE observations could be due to the time-dependence. If we extrapolate the periodicity observed over the past four years, then the RXTE observation coincides with a peak of the sinusoid and should be expected to yield a higher pulse fraction than the time-averaged NICER data. Alternatively, if the time modulation of the pulse fraction is not strictly periodic, then the residual tension could worsen, suggesting a long-term decay of the pulse fraction. Continued monitoring of the pulse fraction oscillation may be able to resolve this uncertainty by determining the stability of the period. In that context we note that if the recent evolution holds, the next peak in pulse

fraction should occur around 2021 September, with the subsequent minimum occurring around 2023 May.

The origin of the variable pulse amplitude is not clear at this time. Because the pulsations of an AMXP are powered by the variable accretion flow, it is generally expected that some of the accretion variability is visible in the pulse waveforms as well. Indeed, the sample of known AMXPs shows ample evidence for such a transfer mechanism. On rapid timescales (seconds), the stochastic and quasi-periodic noise of the accretion disk has been shown to modulate the pulse amplitude (Menna et al. 2003; Bult et al. 2017). Pulse amplitudes also routinely show variations on slower day-long timescales, which are generally understood to be stochastically driven, and are obviously correlated with variations in the source luminosity (Chou et al. 2008), spectroscopy (Kajava et al. 2011), or temporal variability (Bult & van der Klis 2015). The slowly oscillating pulse fraction of IGR J17062 appears to be of a very different nature. Its timescale is much longer than any pulse variability seen in other AMXPs, and notably, it does not correlate with changes in the pulse phase, source luminosity, or any other observable of the accretion system. In particular, the lack of correlation between the pulse fraction and the X-ray flux would suggest that the modulation is not driven by the mass accretion rate. Instead, it may originate in a geometric effect such as a periodic modulation of the apparent size and/or orientation of the stellar hot spot. For instance, it may be that the neutron star is slowly precessing (Zimmermann & Szedenits 1979; Alpar & Pines 1985; Jones & Andersson 2001; Link 2003), although the precession period in AMXPs has been suggested to be on the order of minutes to days (Chung et al. 2008), and presumably would impact the pulse phase as well.

Intriguingly, the only other process in IGR J17062 with a similar timescale is the duty cycle of its intermediate duration X-ray bursts. Assuming no X-ray bursts were missed, the three bursts observed in 2012, 2015, and 2020 give an average burst recurrence time of 1460 days, only somewhat larger than the apparent cycle period observed in the pulse fraction. Both the 2015 and 2020 X-ray bursts occurred near the minima of the pulse fraction. For this relation to extend to the 2012 X-ray burst as well, however, the pulse amplitude oscillation would have to be quasi-periodic, so continued monitoring should be able to establish if these phenomena are truly connected. If, however, they are indeed related, then we can speculate that the changes in the pulse fraction are tied to some physics associated with the deep neutron star crust, rather than the accretion flow.

6.5. *A comparison to other long outbursts*

A remaining open question is why, after two decades in outburst, the pulsations of IGR J17062 are still visible. The two other AMXPs that exhibited a multi-year outburst only showed pulsations for a limited time early

in their outbursts, suggesting that perhaps the decaying pulsations are a feature of prolonged accretion episodes. We briefly discuss how these other two cases compare to IGR J17062.

The best studied case is that of HETE J1900.1–2455 (HETE J1900). This source was first discovered in 2005 June (Vanderspek et al. 2005) and remained in outburst until late 2015 (Degenaar et al. 2017a). Throughout most of its ~ 10 yr outburst, HETE J1900 maintained a high luminosity of about $\sim 4 \times 10^{36}$ erg s $^{-1}$ (Falanga et al. 2007; Papitto et al. 2013), with significant intensity variability throughout (Patruno & Wijmands 2017; Degenaar et al. 2017b). Its 377 Hz pulsations were persistently visible for about 22 days (Kaaret et al. 2006; Galloway et al. 2008), before becoming intermittent and subsequently disappearing entirely (Patruno 2012). This decay has been suggested to be due to magnetic field burial (Cumming 2008), which is supported by the apparent exponential decay in the accretion torque derived from the pulsar timing (Patruno 2012). A particularly strange aspect of HETE J1900 is that during the first two months of outburst its pulse amplitudes appeared to be tied to the occurrences of X-ray bursts: following an X-ray burst, the pulse fraction would abruptly increase and then steadily decay over a ~ 10 day timescale (Galloway et al. 2007).

In IGR J17062 the X-ray bursts might also be occurring when the pulse amplitude is at a minimum, but we did not observe a similar abrupt jump in the pulse fraction following the 2020 burst. The analysis of the NICER epoch containing the X-ray burst complicated by the impact of the X-ray burst cooling tail, though. While the X-ray burst emission dominates, we would not expect to see accretion powered pulsations (see e.g., Watts 2012). The subsequent dip in source intensity suggests that accretion onto the neutron star is inhibited, in which case we might reasonably expect the pulsations to be likewise suppressed. Hence, we would expect that the pulse signal is significantly variable during this time. Unfortunately, however, we lack the sensitivity to test this theory. We find an upper limit on the pulse amplitude of 0.8 – 1.1%, which is comparable to

the pulse fraction we would expect from interpolating the long-term evolution. Hence, we cannot be certain if the pulsations suppressed or if they are present at the expected rate. We can, however, rule out an abrupt factor of $\gtrsim 2$ jump in pulse fraction like the one observed in HETE J1900 (Galloway et al. 2007).

The second case is that of MAXI J0911–655 (MAXI J0911). First discovered in 2016 February (Serino et al. 2016), the outburst of this source is still ongoing. Observations collected during the first month in outburst found 340 Hz pulsations (Sanna et al. 2017b), but these pulsations were no longer visible in observations collected at later times (Bult et al. 2019). In addition to the longevity of its outburst, MAXI J0911 shares a couple of similarities with IGR J17062: it has a 44 minutes ultra-compact binary orbit (Sanna et al. 2017b), and it shows similarly rare but energetic intermediate duration X-ray bursts (Nakajima et al. 2020; Bult et al. 2020b). Where the sources differ, though, is in their luminosity. Like HETE J1900, the luminosity of MAXI J0911 is estimated to be $\sim 5 \times 10^{36}$ erg s $^{-1}$ (Sanna et al. 2017b), an order of magnitude larger than the $\sim 6 \times 10^{35}$ erg s $^{-1}$ luminosity of IGR J17062. Hence, a simple explanation for the persistently visible pulsations of IGR J17062 might be rooted in the much lower luminosity. That is, the magnetic screening process may simply be ineffective at the much lower accretion rate of IGR J17062 (Cumming et al. 2001), or operate on much longer timescales.

Facilities: ADS, HEASARC, NICER

Software: heasoft (v6.27.2), nicerdas (v7a)

ACKNOWLEDGMENTS

This work was supported by NASA through the NICER mission and the Astrophysics Explorers Program, and made use of data and software provided by the High Energy Astrophysics Science Archive Research Center (HEASARC). PB further acknowledges support from the NICER Guest Observer program (80NSSC21K0128) and the CRESST II cooperative agreement (80GSFC17M0002).

REFERENCES

- Alpar, M. A., & Pines, D. 1985, *Nature*, **314**, 334
- Applegate, J. H., & Shaham, J. 1994, *ApJ*, **436**, 312
- Arnaud, K. A. 1996, in *Astronomical Society of the Pacific Conference Series*, Vol. 101, *Astronomical Data Analysis Software and Systems V*, ed. G. H. Jacoby & J. Barnes, **17**
- Bessolaz, N., Zanni, C., Ferreira, J., Keppens, R., & Bouvier, J. 2008, *A&A*, **478**, 155
- Brinkworth, C. S., Marsh, T. R., Dhillon, V. S., & Knigge, C. 2006, *MNRAS*, **365**, 287
- Buccheri, R., Bennett, K., Bignami, G. F., et al. 1983, *A&A*, **128**, 245
- Bult, P., Chakrabarty, D., Arzoumanian, Z., et al. 2020a, *ApJ*, **898**, 38
- Bult, P., & van der Klis, M. 2015, *ApJL*, **798**, L29
- Bult, P., van Doesburgh, M., & van der Klis, M. 2017, *ApJ*, **845**, 124

- Bult, P. M., Arzoumanian, Z., & Gendreau, K. C. 2020b, *The Astronomer's Telegram*, [13760](#), 1
- Bult, P. M., Gendreau, K. C., Strohmayer, T. E., et al. 2019, *The Astronomer's Telegram*, [12869](#), 1
- Burderi, L., Riggio, A., di Salvo, T., et al. 2009, *A&A*, [496](#), [L17](#)
- Chou, Y., Chung, Y., Hu, C.-P., & Yang, T.-C. 2008, *ApJ*, [678](#), [1316](#)
- Chung, C. T. Y., Galloway, D. K., & Melatos, A. 2008, *MNRAS*, [391](#), [254](#)
- Churazov, E., Sunyaev, R., Revnivtsev, M., et al. 2007, *A&A*, [467](#), [529](#)
- Cumming, A. 2008, in *American Institute of Physics Conference Series*, Vol. 1068, *A Decade of Accreting MilliSecond X-ray Pulsars*, ed. R. Wijnands, D. Altamirano, P. Soleri, N. Degenaar, N. Rea, P. Casella, A. Patruno, & M. Linares, [152–159](#)
- Cumming, A., Zweibel, E., & Bildsten, L. 2001, *ApJ*, [557](#), [958](#)
- Degenaar, N., Altamirano, D., & Wijnands, R. 2012, *The Astronomer's Telegram*, [4219](#), 1
- Degenaar, N., Miller, J. M., Wijnands, R., Altamirano, D., & Fabian, A. C. 2013, *ApJL*, [767](#), [L37](#)
- Degenaar, N., Ootes, L. S., Reynolds, M. T., Wijnands, R., & Page, D. 2017a, *MNRAS*, [465](#), [L10](#)
- Degenaar, N., Pinto, C., Miller, J. M., et al. 2017b, *MNRAS*, [464](#), [398](#)
- di Salvo, T., Burderi, L., Riggio, A., Papitto, A., & Menna, M. T. 2008, *MNRAS*, [389](#), [1851](#)
- Di Salvo, T., & Sanna, A. 2020, [arXiv e-prints](#), [arXiv:2010.09005](#)
- Falanga, M., Poutanen, J., Bonning, E. W., et al. 2007, *A&A*, [464](#), [1069](#)
- Friedman, J. L., Ipser, J. R., & Parker, L. 1986, *ApJ*, [304](#), [115](#)
- Galloway, D. K., Morgan, E. H., & Chakrabarty, D. 2008, in *American Institute of Physics Conference Series*, Vol. 1068, *A Decade of Accreting MilliSecond X-ray Pulsars*, ed. R. Wijnands, D. Altamirano, P. Soleri, N. Degenaar, N. Rea, P. Casella, A. Patruno, & M. Linares, [55–62](#)
- Galloway, D. K., Morgan, E. H., Krauss, M. I., Kaaret, P., & Chakrabarty, D. 2007, *ApJL*, [654](#), [L73](#)
- Ginzburg, S., & Quataert, E. 2020, *MNRAS*, [495](#), [3656](#)
- Hartman, J. M., Patruno, A., Chakrabarty, D., et al. 2008, *ApJ*, [675](#), [1468](#)
- Hernández Santisteban, J. V., Cúneo, V., Degenaar, N., et al. 2019, *MNRAS*, [488](#), [4596](#)
- Illarionov, A. F., & Sunyaev, R. A. 1975, *A&A*, [39](#), [185](#)
- Ingram, A., van der Klis, M., Middleton, M., Altamirano, D., & Uttley, P. 2017, *MNRAS*, [464](#), [2979](#)
- Iwakiri, W., Keek, L., Serino, M., et al. 2015, *The Astronomer's Telegram*, [8253](#), 1
- Jones, D. I., & Andersson, N. 2001, *MNRAS*, [324](#), [811](#)
- Justham, S., Rappaport, S., & Podsiadlowski, P. 2006, *MNRAS*, [366](#), [1415](#)
- Kaaret, P., Morgan, E. H., Vanderspek, R., & Tomsick, J. A. 2006, *ApJ*, [638](#), [963](#)
- Kajava, J. J. E., Ibragimov, A., Annala, M., Patruno, A., & Poutanen, J. 2011, *MNRAS*, [417](#), [1454](#)
- Keek, L., Iwakiri, W., Serino, M., et al. 2017, *ApJ*, [836](#), [111](#)
- Kraft, R. P., Mathews, J., & Greenstein, J. L. 1962, *ApJ*, [136](#), [312](#)
- Link, B. 2003, in *Astronomical Society of the Pacific Conference Series*, Vol. 302, *Radio Pulsars*, ed. M. Bailes, D. J. Nice, & S. E. Thorsett, [241](#)
- Long, M., Romanova, M. M., & Lovelace, R. V. E. 2005, *ApJ*, [634](#), [1214](#)
- Markwardt, C. B., Swank, J. H., Strohmayer, T. E., in 't Zand, J. J. M., & Marshall, F. E. 2002, *ApJL*, [575](#), [L21](#)
- Menna, M. T., Burderi, L., Stella, L., Robba, N., & van der Klis, M. 2003, *ApJ*, [589](#), [503](#)
- Nakajima, M., Sugita, S., Serino, M., et al. 2020, *The Astronomer's Telegram*, [13754](#), 1
- Negoro, H., Serino, M., Sasaki, R., et al. 2015, *The Astronomer's Telegram*, [8241](#), 1
- Nelson, L. A., & Rappaport, S. 2003, *ApJ*, [598](#), [431](#)
- Nishida, H., Serino, M., Iwakiri, W., et al. 2020, *The Astronomer's Telegram*, [13827](#), 1
- Papitto, A., D'Ai, A., Di Salvo, T., et al. 2013, *MNRAS*, [429](#), [3411](#)
- Patruno, A. 2012, *ApJL*, [753](#), [L12](#)
- Patruno, A., & Wijnands, R. 2017, [arXiv e-prints](#), [arXiv:1706.03354](#)
- Patruno, A., Wijnands, R., & van der Klis, M. 2009, *ApJL*, [698](#), [L60](#)
- Patruno, A., Jaodand, A., Kuiper, L., et al. 2017, *ApJ*, [841](#), [98](#)
- Poutanen, J., & Gierliński, M. 2003, *MNRAS*, [343](#), [1301](#)
- Psaltis, D., & Chakrabarty, D. 1999, *ApJ*, [521](#), [332](#)
- Rappaport, S., Joss, P. C., & Webbink, R. F. 1982, *ApJ*, [254](#), [616](#)
- Rappaport, S., Nelson, L. A., Ma, C. P., & Joss, P. C. 1987, *ApJ*, [322](#), [842](#)
- Rappaport, S., Verbunt, F., & Joss, P. C. 1983, *ApJ*, [275](#), [713](#)
- Rappaport, S. A., Fregeau, J. M., & Spruit, H. 2004, *ApJ*, [606](#), [436](#)
- Remillard, R. A., & Levine, A. M. 2008, *The Astronomer's Telegram*, [1853](#), 1

- Ricci, C., Beckmann, V., Carmona, A., & Weidenspointner, G. 2008, *The Astronomer's Telegram*, [1840](#), [1](#)
- Richman, H. R., Applegate, J. H., & Patterson, J. 1994, *PASP*, [106](#), [1075](#)
- Romanova, M. M., Ustyugova, G. V., Koldoba, A. V., & Lovelace, R. V. E. 2005, *ApJL*, [635](#), [L165](#)
- Rosen, S. 2020, Status of the EPIC-pn absolute timing capabilities using the Crab pulsar, Tech. Rep. XMM-SOC-CAL-TN-220, ESA/XMM-SOC
- Salmi, T., Nättilä, J., & Poutanen, J. 2018, *A&A*, [618](#), [A161](#)
- Sanna, A., Papitto, A., Burderi, L., et al. 2017a, *A&A*, [598](#), [A34](#)
- Sanna, A., Di Salvo, T., Burderi, L., et al. 2017b, *MNRAS*, [471](#), [463](#)
- Serino, M., Tanaka, K., Negoro, H., et al. 2016, *The Astronomer's Telegram*, [8872](#), [1](#)
- Standish, E. M. 1998, *JPL Interoffice Memorandum*, [312](#), [98](#)
- Steiner, A. W., Gandolfi, S., Fattoyev, F. J., & Newton, W. G. 2015, *PhRvC*, [91](#), [015804](#)
- Strohmayer, T., & Keek, L. 2017, *ApJL*, [836](#), [L23](#)
- Strohmayer, T. E., Arzoumanian, Z., Bogdanov, S., et al. 2018, *ApJL*, [858](#), [L13](#)
- Tavani, M., & London, R. 1993, *ApJ*, [410](#), [281](#)
- Ustyugova, G. V., Koldoba, A. V., Romanova, M. M., & Lovelace, R. V. E. 2006, *ApJ*, [646](#), [304](#)
- van den Eijnden, J., Degenaar, N., Pinto, C., et al. 2018, *MNRAS*, [475](#), [2027](#)
- Vanderspek, R., Morgan, E., Crew, G., Graziani, C., & Suzuki, M. 2005, *The Astronomer's Telegram*, [516](#), [1](#)
- Verbunt, F. 1993, *ARA&A*, [31](#), [93](#)
- Watts, A. L. 2012, *ARA&A*, [50](#), [609](#)
- Wilms, J., Allen, A., & McCray, R. 2000, *ApJ*, [542](#), [914](#)
- Zanni, C., & Ferreira, J. 2013, *A&A*, [550](#), [A99](#)
- Zimmermann, M., & Szedenits, E., J. 1979, *PhRvD*, [20](#), [351](#)

APPENDIX

A. SEMI-COHERENT SEARCH RESULTS

Table A1 lists the detailed search results of the per-epoch Z_1^2 pulse searches applied to the NICER observations.

Table A1. Semi-coherent search results

Group	$\Delta\nu$ (mHz)	T_{asc} (TDB)	Z_1^2
1	0.48 ± 0.11	$57977.43825 \pm 1.5 \times 10^4$	130.67
2	0.8 ± 0.4	$58049.31841 \pm 2.0 \times 10^4$	66.96
3	0.51 ± 0.07	$58062.44916 \pm 1.2 \times 10^4$	153.39
6	0.71 ± 0.11	$58588.78465 \pm 1.1 \times 10^4$	179.50
7	0.5 ± 0.4	$58668.99685 \pm 2.5 \times 10^4$	40.28
8	0.90 ± 0.5	$58786.01840 \pm 3.0 \times 10^4$	22.40
10	0.97 ± 0.05	$59067.23529 \pm 1.1 \times 10^4$	163.92

NOTE—Spin frequency and time of ascending node measurements obtained through the Z_1^2 optimization search. The frequencies are expressed relative to a reference frequency as $\Delta\nu = \nu - \nu_{\text{ref}}$, where $\nu_{\text{ref}} = 163.656110$ Hz.

B. PHASE-AVERAGED SPECTROSCOPY

Table B2 lists the detailed best-fit spectral parameters obtained from the per-epoch spectroscopic analysis of out NICER observations.

Table B2. Phase-averaged spectroscopic results

Group	E_{line} (keV)	σ_{line} (keV)	F_{Gaussian}	BB Norm (km / 10 kpc) ²	BB Temp (keV)	Γ	F_{PL}
1	0.943 ± 0.006	0.210 ± 0.007	0.158 ± 0.009	79 ± 4	0.396 ± 0.004	1.784 ± 0.012	3.75 ± 0.04
2	0.952 ± 0.006	0.191 ± 0.007	0.175 ± 0.010	71 ± 4	0.419 ± 0.005	1.747 ± 0.013	4.70 ± 0.06
3	0.945 ± 0.006	0.198 ± 0.008	0.144 ± 0.008	68 ± 3	0.421 ± 0.004	1.821 ± 0.012	3.86 ± 0.05
4	0.919 ± 0.021	0.228 ± 0.022	0.178 ± 0.025	65 ± 7	0.432 ± 0.012	1.804 ± 0.030	3.08 ± 0.13
5	0.968 ± 0.012	0.167 ± 0.015	0.143 ± 0.017	82 ± 6	0.424 ± 0.008	1.845 ± 0.022	4.10 ± 0.12
6	0.979 ± 0.005	0.174 ± 0.006	0.148 ± 0.007	73 ± 3	0.425 ± 0.004	1.885 ± 0.010	5.36 ± 0.05
7	0.965 ± 0.003	0.170 ± 0.004	0.163 ± 0.005	80.9 ± 1.9	0.428 ± 0.002	1.820 ± 0.010	4.60 ± 0.04
8	0.954 ± 0.005	0.195 ± 0.006	0.143 ± 0.006	74.7 ± 2.1	0.416 ± 0.003	1.867 ± 0.011	3.21 ± 0.03
10	0.962 ± 0.003	0.181 ± 0.003	0.153 ± 0.004	80.9 ± 1.5	0.412 ± 0.002	1.826 ± 0.010	3.91 ± 0.02

NOTE—The absorption column density is $N_H = (0.107 \pm 0.002) \times 10^{22} \text{ cm}^{-2}$, and was tied across the different groups. The Gaussian flux (F_{Gaussian}) and power law flux (F_{PL}) are measured in the 1 – 10 keV band and expressed in units of $10^{-11} \text{ erg s}^{-1} \text{ cm}^{-2}$.